NANOPARTICLE SYNTHESIS AND CHARACTERIZATION OF Li–Mg–Al FERRITES: POTENTIAL APPLICATIONS IN CAPACITOR AND MAGNETIC STORAGE MEDIA

Sachin S. Tirlapur [1], Vinut V. Tambe [1], Sushant S. Kakati [2], Shridhar N. Mathad [2], Sangamesh V. Angadi [1], Deepak B. Shirgaonkar [3], Appanna S. Pujar [4], Satyappa L. Galagali [4], Pundalik R. Jeeragal [1], Chidanandayya S. Hiremath [5], Rangappa B. Pujar [1]

[1] Department of Physics
P. C. Jabin Science College
Hubballi, Karnataka, India
[2] Department of Engineering Physics
K. L. E. Institute of Technology
Hubballi, Karnataka, India
physicssiddu@kleit.ac.in
physicssiddu@gmail.com
[3] Department of Physics
Anandibai Raorane Arts, Commerce and Science College
Vaibhavwadi, Maharastra, India
[4] Department of Physics
R. L. S. Institute
Belagavi, Karanataka, India
[5] Department of Physics
S. K. Arts and H. S. Kotambari Science Institute
Hubballi, Karnataka, India

Accepted 7 August 2023

Abstract

This study presents the synthesis and characterization of $Li_{0.50}Mg_{0.75}Al_xFe_{2-x}O_4$ ferrite nanoparticles, where x varies from 0.15 to 0.60. The synthesized nanoparticles were characterized using X-ray diffraction (XRD), scanning electron microscopy (SEM) with energy-dispersive X-ray analysis (EDX), Fourier-transform infrared (FTIR) spectroscopy, dielectric properties and vibrating sample magnetometry (VSM). The XRD analysis showed that all the samples have a single-phase fcc spinel structure. The SEM images revealed the formation of spherical nanoparticles with a size range of 11–39 nm. EDX analysis confirmed the presence of constituent elements and Al substitution. FTIR spectra indicated the characteristic vibrational frequencies corresponding to metal–oxygen bonds in the spinel structure. The dielectric properties of the samples were studied as a function of frequency and temperature. The dielectric constant and dielectric loss showed a decrease with an increase in frequency. The VSM measurements showed that all the samples exhibit ferrimagnetic behavior. The magnetic properties were observed to be dependent on Al substitution with a decrease in saturation magnetization. The results indicate that $Li_{0.50}Mg_{0.75}Al_xFe_{2-x}O_4$ nanoparticles have potential applications in various fields such as capacitors, and magnetic storage media.

1. Introduction

Magnetic materials have become an integral part of modern technology due to their extensive applications in various fields such as data storage, power generation, and electronics. Ferrites, in particular, have emerged as a promising candidate for various magnetic applications due to their unique magnetic and electrical properties. Ferrites are a type of ceramic material composed of iron oxide and other metal oxide, typically with a spinel structure [**1**].

One of the major limitations of ferrites is their low electrical conductivity, which restricts their use in certain applications. To overcome this limitation, various dopants have been added to the ferrite matrix, which not only enhances their electrical conductivity but also alters their magnetic properties [**2**]. Among these dopants, Al-doping has been extensively studied due to its unique properties and ability to enhance the electrical conductivity and magnetic properties of ferrites [**3**].

Li–Mg ferrites, a type of spinel ferrite, have gained significant attention due to their excellent magnetic properties, including high magnetic anisotropy and large saturation magnetization [**4**]. They have been widely used in various applications, including microwave devices, power transformers, and magnetic recording media. However, limited electrical conductivity has restricted their application in certain areas. Al-doping has emerged as a potential solution to this limitation, as it not only enhances the electrical conductivity of Li–Mg ferrites but also alters their magnetic properties [**5**].

The addition of Al-dopant to Li–Mg ferrites results in a significant improvement in their electrical conductivity due to the substitution of Al ions for Fe ions in the ferrite lattice. This substitution results in the formation of oxygen vacancies and Fe^{3+} ions, which act as charge carriers and contribute to the enhancement of electrical conductivity. Moreover, Al-doping also alters the magnetic properties of Li–Mg ferrites, leading to an increase in their saturation magnetization, magnetic anisotropy, and magnetic susceptibility. The electrical and magnetic properties of Al-doped Li–Mg ferrites depend on several factors, including the amount of dopant added, sintering temperature, and processing conditions. Therefore, a detailed understanding of the effects of these factors on the properties of Al-doped Li–Mg ferrites is essential for their successful application in various fields [**5 – 7**].

In recent years, several studies have been conducted on the synthesis and characterization of Al-doped Li–Mg ferrites, with a focus on understanding the impact of Al-doping on their electrical and magnetic properties. These studies have shown that Al-doping can significantly enhance the electrical conductivity of Li–Mg ferrites while simultaneously altering their magnetic properties. The results of these studies have paved the way for the development of Al-doped Li–Mg ferrites with tailored properties for various applications [**8**].

Finally, Al-doped Li–Mg ferrites have emerged as a promising candidate for various magnetic applications due to their unique electrical and magnetic properties. The addition of Al-dopant to Li–Mg ferrites enhances their electrical conductivity and alters their magnetic properties, making them suitable for use in various fields. Further research is required to fully understand the impact of Al-doping on the properties of Li–Mg ferrites and to develop optimized materials for specific applications.

 https://doi.org/10.52340/ns.2022.23.24.03

2. Experimental

The sol–gel auto combustion method is a process used to synthesize ceramic materials. In the case of $Li_{0.50}Mg_{0.75}Al_xFe_{2-x}O_4$ (x = 0.15, 0.30, 0.45, and 0.60), this method can be used to prepare spinel ferrites with varying amounts of aluminum and iron. The synthesis process involves several steps:

Step 1: Sol preparation – metal nitrates $LiNO_3$, $Mg(NO_3)_2$, $Al(NO_3)_3{\cdot}9H_2O$, and $Fe(NO_3)_3{\cdot}9H_2O$ are dissolved, usually, in water. A fuel molecule (such as glycine) is added to the solution, which serves as a reducing agent during the combustion process. The solution is mixed thoroughly to ensure uniformity.

Step 2: Gel formation – the solution obtained is heated slowly to evaporate the water and promote gel formation. This process leads to the formation of a gel, which contains a network of interconnected particles that consist of metal ions and fuel molecules. The chemical reaction can be represented as follows:

$$\text{metal oxides} + \text{fuel} \rightarrow \text{gel}$$

Step 3: Auto-combustion – the gel is heated rapidly to initiate the combustion process. The fuel molecules burn, releasing energy in the form of heat causing a rapid increase in temperature, leading to the combustion of the remaining fuel molecules and the transformation of the metal oxides into the desired spinel structure. The chemical reaction can be represented as follows:

$$\text{gel} + \text{heat} \rightarrow \text{spinel structure} + CO_2 + H_2O + N_2$$

Step 4: Calcination – the combustion resulting product is calcined (heated in air or oxygen) to remove any remaining organic compounds and to further stabilize the spinel structure.

The specific values of x used in the synthesis of $Li_{0.50}Mg_{0.75}Al_xFe_{2-x}O_4$ determine the amounts of aluminum and iron in the final product. For example, when x = 0.15, the final product contains 0.15 M of aluminum and 1.85 M of iron for every 2 M of metal ions. The specific chemical reactions for value of x are as follows:

$$LiNO_3 + Mg(NO_3)_2 + Al(NO_3)_3{\cdot}9H_2O + Fe(NO_3)_3{\cdot}9H_2O + \text{glycine} \rightarrow$$
$$\rightarrow Li_{0.50}Mg_{0.75}Al_x5Fe_{2-x}O_4 + CO_2 + H_2O + N_2$$

As x increases, the amount of aluminum in the final product increases, while the amount of iron decreases. Overall, the sol–gel auto combustion method is a versatile technique for synthesizing ceramic materials with controlled compositions and properties.

3. Results and discussion

3.1. Structural characteristics

The samples are mixed spinel oxides that have different amounts of the cations aluminum Al and iron Fe in their crystal structure, which is $Li_{0.50}Mg_{0.75}Al_xFe_{2-x}O_4$, x = 0.15, 0.30, 0.45, and 0.60. The crystal system has the space group Fd-3m and is cubic. All four XRD patterns exhibit a number of strong peaks at low angles, which denotes the presence of well-crystallized materials. In **Figure 1a**, around $2\theta = 36°$, which corresponds to the spinel structure's (311) plane, is where

the peak with the highest intensity may be seen. Other prominent peaks are observed at around 2θ = 30 to 63° angle, corresponding to the planes, respectively. It is possible to identify the crystal structure of all samples as cubic spinels with lattice parameters ranging from 8.136 to 8.346 Å by examining the peak positions and intensities. Because Fe has a greater atomic radius than Al, the lattice parameter initially increases as the concentration of Fe in the lattice grows, as shown in **Table 1** by the rising Al and Fe cations substitution. The lattice parameter rises as a result of the greater atomic radius of Fe atoms, which increases the space between repeating units in the crystal lattice. Vegard's law, which stipulates that the lattice parameter of a solid solution is a linear function of the concentration of the constituent atoms, is broken in this event, which is referred to as positive deviation from Vegard's law.

Table 1. Data on lattice constant, average particle size, dislocation density, lattice strain and X-ray density, porosity.

Composition x	Lattice constant a, Å	Average particle size D, nm	Dislocation density, $\times 10^{12}$ m^2	Lattice strain, $\times 10^{-30}$	X-ray density d_x, g/cm^3	Porosity, %
0.15	8.136	38.90	660	0.94	2.699	66.76
0.30	8.338	24.89	1614	1.39	2.498	71.50
0.45	8.346	26.11	1460	1.33	2.481	69.32
0.60	8.327	10.80	8573	3.24	2.488	68.48

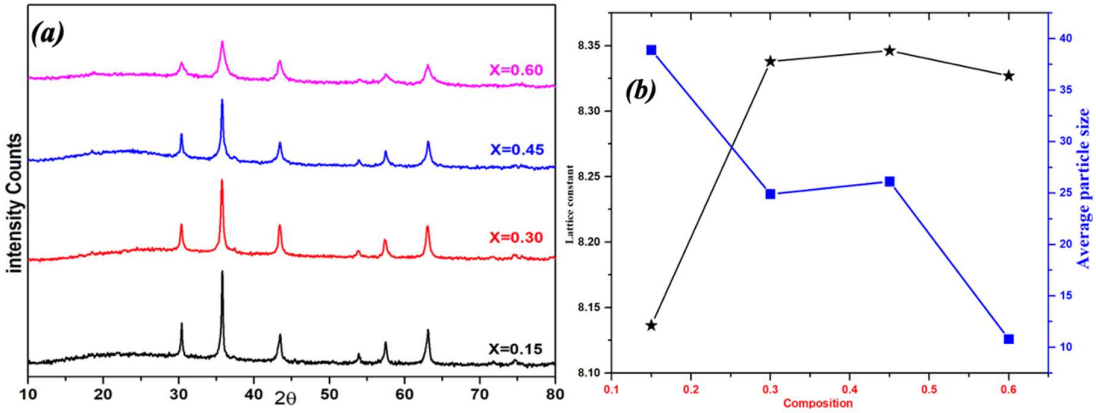

Figure 1. XRD patterns and lattice constants of $Li_{0.50}Mg_{0.75}Al_xFe_{2-x}O_4$.

However, at a concentration of x = 0.60, the lattice parameter decreases due to the creation of Fe-rich areas in the crystal lattice, which is triggered by the rising Fe concentration. This alteration of the crystal structure in these locations can cause the lattice parameter to drop. This is referred to as a negative departure from Vegard's law because it shows that the lattice parameter does not increase linearly with the atom concentration, as shown in **Figure 1(b)**.

Some parameters can be calculated using formulas such as the interplanar distance of a cubic system, which can be calculated using an equation **[1, 9]**:

$$d = \frac{a}{\sqrt{h^2 + k^2 + l^2}}$$

[10], where, a is the lattice constant, (hkl) are the Miller indices and the lattice constant is calculated by using the relation,

https://doi.org/10.52340/ns.2022.23.24.03

$$a = \frac{\lambda}{2\sin\theta}\sqrt{h^2 + k^2 + l^2},$$

where λ = wavelength and θ = glancing angle. The major line in diffraction pattern corresponds to plane (311). Knowing these values, lattice constant can be calculated. The standard particle size of a sample is given by the relation,

$$D \approx \frac{0.9\,\lambda}{\beta\cos\theta},$$

[11], where, β = full width half-maximum corresponding to plane of (311). Like-wise, the dislocation density ρ, lattice strain ε and porosity P can be calculated:

$$\rho = \frac{1}{D^2},$$

$$\varepsilon = \frac{\beta\cos\theta}{4},$$

$$P = \frac{d_x - d_a}{d_x} \times 100\%,$$

where X-ray density

$$d_x = \frac{ZM}{Na^3},$$

where Z = number of molecules per unit cell, M = molecular mass, N = Avogadro's number (≈6.022×10^{23}), a = lattice constant, and d_a = actual density.

The variation of crystallite size with composition depicted on the **Table 1**. It is observed that the crystallite size varies from 11 to 39 nm. The size is found to decrease with increase in composition of Al. Because Al has a smaller atomic radius than Fe, the size of the crystallites tends to decrease as the percentage of Al increases. Al distorts the lattice structure when it is introduced to a crystal, which can lead to the development of smaller crystallites. The "grain-refining effect" of Al is the name given to this effect [12]. The deformation in the lattice structure gets worse as the Al concentration rises, which causes the size of the crystallites to shrink even more. This is due to the fact that the presence of Al atoms causes areas with a high density of lattice defects, which serve as nucleation sites for the growth of smaller crystallites. Differences in the preparation process, sample purity, and sintering temperature utilized to prepare the material can be blamed for the porosity range from 66 to 71%.

3.2. FTIR Results

The FTIR spectra of the samples showed characteristic peaks at different frequencies, indicating the presence of different functional groups. The peaks observed in the **Table 2** to identify the functional groups present in the material. The peaks observed at 535–549 cm^{-1} can be attributed to the stretching vibration ν_1 of the tetrahedral site in the spinel structure. The peaks observed at 498–621 cm^{-1} can be attributed to the stretching vibration ν_2 of the octahedral site in the spinel structure. The slight change in the frequency with composition may be due to the change in Fe^{3+}–O^{2-} distances in the octahedral and tetrahedral complexes. Jahn–Teller effect results in the splitting of bands ν_1 and ν_2 due to presence of Fe^{2+}, which locally produces deformation in the lattice due to a non-cubic component of the crystal field potential. The peaks observed at 1500–1650 cm^{-1} can be attributed to the bending vibration of the water molecule adsorbed on the surface of the sample [13]. The peak observed at 3430 cm^{-1} can be attributed to the O–H stretching vibration of the hydroxyl group (–OH) present on the surface of the sample.

Table 2. Data on FTIR absorption bands of $Li_{0.50}Mg_{0.75}Al_xFe_{2-x}O_4$ ferrites.

Composition	Absorption bands	
x	ν_1, cm^{-1}	ν_2, cm^{-1}
0.15	535	498
0.30	546	522
0.45	544	520
0.60	549	521

From the FTIR spectra, it can be concluded that all the samples have similar chemical bonding and functional groups. They did not show any significant differences with varying values of x. This suggests that the substitution of Al and Fe in the spinel structure did not significantly affect the chemical bonding and functional groups present in the material [**14**].

3.3. Scanning electron microscope analysis

The SEM micrographs represented in **Figure 2** reveal the samples porosity ranging from 66 to 71%, while the grain size varies from 16 to 25 μm depending on the applied heat treatment.

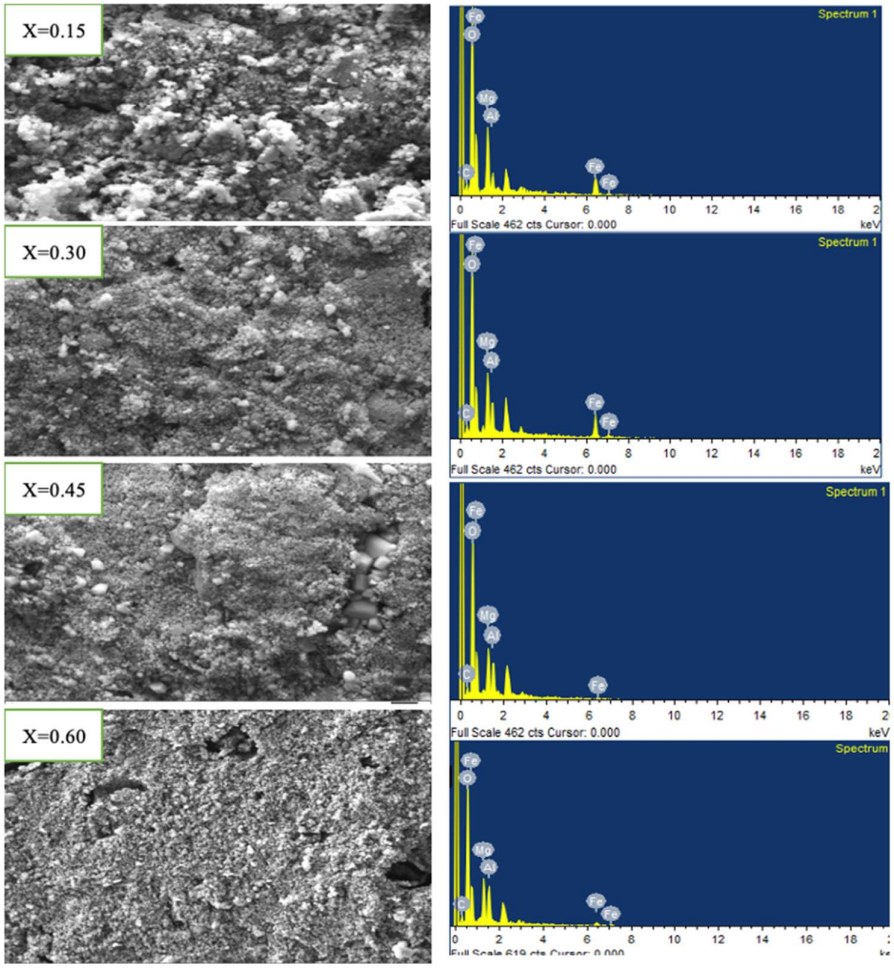

Figure 2. SEM and EDAX spectrum of $Li_{0.50}Mg_{0.75}Al_xFe_{2-x}O_4$ ferrites.

https://doi.org/10.52340/ns.2022.23.24.03

Table 3. Data on X-ray density, actual density, and porosity.

Composition x	Average grain diameter D, μm	Actual density, g/cm³	X-ray density d_x, g/cm³	Porosity, %
0.15	18.52	0.896	2.699	66.8
0.30	17.29	0.712	2.498	71.5
0.45	16.20	0.762	2.481	69.3
0.60	25.56	0.784	2.488	68.5

The maximum grain size is observed in the sample composition x = 0.60, which is attributed to unequal diffusion rates causing porosity development at the neck base. This mechanism leads to the characteristic microstructure of ferrites where residual porosity appears in intra-granular space. The calculated data indicates that an increase in Al composition results in a decrease in the average grain size, owing to the presence of metal ion vacancies caused by oxidation of suitable doping [**15**]. The EDX sample peaks shown in **Figure 2** reveal the formation of an fcc structure with impurities from the atmosphere. The identified elements from the EDX analysis include Mg, Al, Fe, and O, while Li is absent due to the limitations of the EVO MA18 machine with Oxford EDS (X-act) in detecting elements with atomic numbers less than carbon. Overall, the SEM micrographs and EDX analysis provide valuable insights into the microstructure and elemental composition of the samples (**Table 3**), highlighting the effects of heat treatment and Al composition in determining the grain size and porosity of ferrites [**16**].

3.4. Dielectric properties analysis

By using the two probe approach, the sample in pellet form is utilized to measure capacitance C_p and dielectric loss ε at room temperature in the frequency range of 20 Hz to 1 MHz. By using the relation, the dielectric constant is computed:

$$\varepsilon = \frac{C_p t}{\varepsilon_0 A},$$

where A is the area of the pellet cross section, C_p is the capacitance of a parallel plate capacitor, t is the thickness of the pellet, and ε_0 is the permittivity of empty space in SI units.

The dielectric relaxation brought on by localized electric charges is related to the AC conductivity σ_{AC}. From the relationship, the frequency dependent AC conductivity is derived:

$$\sigma_{AC} = 2\pi f \varepsilon_0 \varepsilon,$$

where f is the frequency of the applied electric field, ε_0 is the permittivity of free space in SI units, and ε is the dielectric constant.

In this prepared materials the dielectric properties (**Table 4** and **Figure 3**) of ferrites in the frequency range of 20 Hz to 1 MHz. It mentions that the dispersion in dielectric constant is due to Maxwell's–Wagner polarization and space charge polarization at grain boundaries, interfacial dislocation, oxygen vacancies, grain defects, and the predominance of large Fe^{3+} ions. This means that the polarization of the material lags behind the external applied field due to the presence of these factors. Due to the presence of more free charge carriers, the material's conductivity may

increase as a result of the increase in porosity growth from 66 to 71%. A material's conductivity increases with the amount of vacant space it contains since this gives electrons greater room to roam around freely. In fact, the analysis' findings demonstrate that as the material's porosity rose from 66 to 71%, its AC conductivity increased from 2896 to 21640 Sm.

Table 4. Data on porosity and AC conductivity at 1 MHz.

Composition, x	Lattice constant a, Å	Porosity, %	AC conductivity σ, Sm
0.15	8.136	66.76	2896
0.30	8.338	71.50	21640
0.45	8.346	69.32	7750
0.60	8.327	68.48	7526

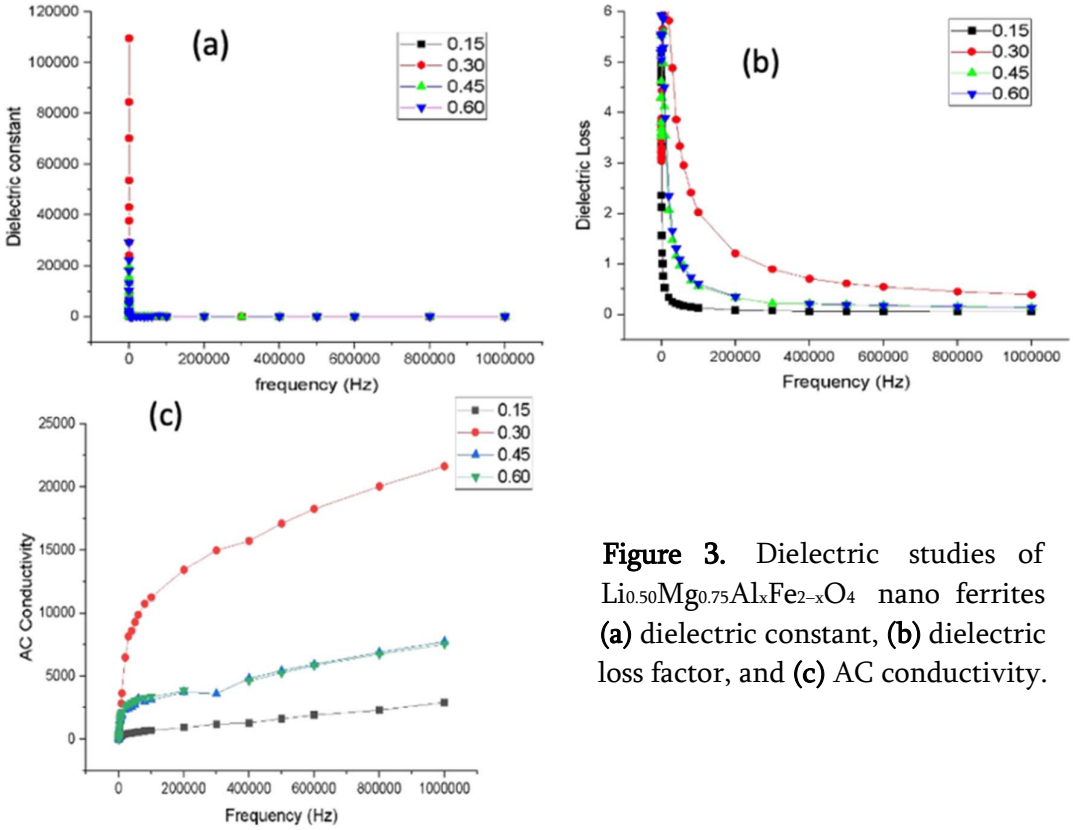

Figure 3. Dielectric studies of $Li_{0.50}Mg_{0.75}Al_xFe_{2-x}O_4$ nano ferrites **(a)** dielectric constant, **(b)** dielectric loss factor, and **(c)** AC conductivity.

The increased porosity Al-doped Li–Mg ferrites may be used for applications requiring high electrical conductivity, such as electrical wiring or electronic components, based on the increase in conductivity [**17**]. At lower frequencies, the grain boundaries are active to a greater extent than the grains, while at higher frequencies only grains are active in electrical conduction [**18**]. The variation of relative dielectric permittivity can be related to the collective behavior of both types of electronic charge carriers, electrons and holes [**19, 20**]. The dielectric loss arises when polarization lags behind the applied alternating field due to impurity and imperfection in crystal lattice [**21**]. This means that the material is not able to follow the applied field immediately,

https://doi.org/10.52340/ns.2022.23.24.03

resulting in a loss of energy and upper limit loss (maximum) takes place when the period of relaxation is alike to the period of the applied field.

On the basis of Koops' phenomenological theory, dielectric dispersion means the dependence of the permittivity of a dielectric material on the frequency of applied electric field. Because of ever lagging relation between change in polarization and change in electric field, the permittivity of dielectric is a complex valued function of frequency and hence domain wall resonance loss factor curve is originated [**22, 23**]. Austin and Mott hopping model proposed conductivity of ferrites is due to electrons and polarons and conduction mechanism is governed by the hopping length, which is the distance between ions in site A and B. The inverse tangential increase in conductivity with frequency is attributed to small polaron, which means that the conductivity decreases as the frequency increases. In this analysis we discusses the factors that cause polarization lag, porosity, dielectric loss, and conductivity in ferrites [**21 – 23**]. This loss factor curve is caused by ion migration losses, electron polarization losses and dipole relaxation losses. At higher frequencies the losses are found to be low if domain wall motion is inhibited and magnetization is forced to change by rotation due to domain wall resonance [**22 – 24**].

3.5. Magnetic properties analysis

The observed variation of saturation magnetization vs. alternating magnetizing field of the samples are shown in **Figure 4**. Both Al and Li are nonmagnetic elements. As composition of Al increases, the amount of Fe^{3+} ions on both A and B sites decreases, and results in reduction of magnetization with increase in aluminum composition. Magnetic properties of ferrites depend on chemical composition, porosity, grain size, and interaction between tetrahedral and octahedral sites. In ferrites, the variation in saturation magnetization has been attributed to both surface spin effect, density composition of sample and cation distribution on A and B sites [**26**]. A–B interaction gets weakened causing the decrease in saturation magnetization increase in aluminum Al content. Few other factors that influences the magnetization of ferrites is microstructure: each sample grain has certain magnetic moment, the presence of pores breaks the magnetic circuits among the grains, which leads to the net decreases in magnetic moment, with increase in porosity. At higher sintering temperatures, small numbers of large grains are produced and consequently porosity is decreases [**26 – 28**].

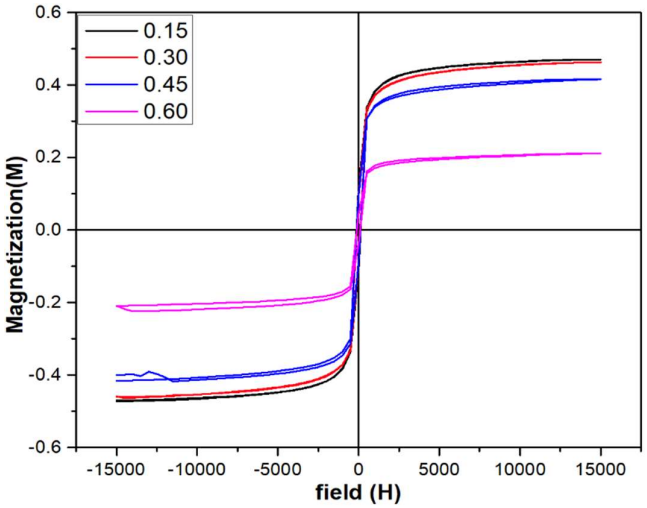

Figure 4. Magnetic properties study of $Li_{0.50}Mg_{0.75}Al_xFe_{2-x}O_4$ nano ferrites.

Table 5. Different magnetic parameters for all Al-substituted Li–Mg ferrites.

Composition x	Molecular mass M	Saturation magnetization M_s, emu/g	Coercive field H_c, Oe	Magnetic moment μ_B, N·m	Porosity, %
0.15	193	0.473	127	0.0163	66.8
0.30	188	0.465	109	0.0157	71.5
0.45	184	0.418	115	0.0138	69.3
0.60	180	0.129	97	0.0070	68.5

Table 5 provides information on saturation magnetization, magnetic moment μ_B, and coercive field H_c.

4. Conclusions

1. The XRD analysis revealed distinct diffraction peaks confirming the formation of single-phase spinel structures in the Al-substituted Li–Mg ferrites.
2. SEM images showed uniform and well-defined nano-sized particles with an average grain size of 18 to 25 μm, and EDX analysis confirmed the successful incorporation of aluminum into the ferrite lattice.
3. The FTIR spectra exhibited characteristic absorption bands at 498 and 549 cm^{-1}, corresponding to the tetrahedral and octahedral complexes of the ferrites, respectively.
4. The dielectric constant of the nano-sized ferrites displayed a strong frequency dependence on following Koops' theory. The significant increase in AC conductivity from 2896 to 21640 Sm makes the porosity Al-doped Li–Mg ferrites suitable for high electrical conductivity applications like electrical wiring and electronic components.
5. Al composition in ferrites reduces magnetization due to fewer Fe^{3+} ions on A and B sites. Magnetic properties depend on composition (x = 0.15 to 0.60), porosity (61 to 71%). A–B interaction weakens with higher Al content, lowering saturation magnetization ranging from 0.473 to 0.129.

References

[1] S. K. Sushant, N. J. Choudhari, S. Patil, M. K. Rendale, S. N. Mathad, A. T. Pathan. Development of M–$NiFe_2O_4$ (Co, Mg, Cu, Zn, and rare earth materials) and the recent major applications. Int. J. SHS, 2023, 32 (2), 61-116.

[2] N. J. Choudhari, S. S. Kakati, C. S. Hiremath, R. B. Pujar. Structure dependent electrical properties of Ni–Mg–Cu nano ferrites. AIP Conf. Proc., 2016, 1728, 020153 (1-7).

[3] M. K. Rendale, S. N. Mathad, D. C. Kulkarni, V. Puri. Dielectric and magnetic properties of substituted Li–Zn ferrite thick films clouded over a half wavelength microstrip rejection filter. Int. J. SHS, 2016, 25 (2), 86-91.

[4] M. Asifiqbal, M. U. Islam, I. Ali, M. A. Khan, Sh. M. Ramay, M. H. Khan, M. Khalid Mehmood. Study of physical, magnetic and electrical properties of rare-earth substituted Li–Mg ferrites. J. Alloys Comp., 2017, 692, 322-331.

 https://doi.org/10.52340/ns.2022.23.24.03

[5] S. P. Waghmare, D. M. Borikar, K. G. Rewatkar. Impact of Al doping on structural and magnetic properties of Co–ferrite. Mater. Today Proc., 2017, 4 (11), 11866-11872.

[6] M. S. Hasan, M. I. Arshad, A. Ali, K. Mahmood, N. Amin, S. S. Ali, M. I. Khan, G. Mustafa, M. J. Khan, M. Saleem. Mg and La co-doped ZnNi spinel ferrites for low resistive applications. Mater. Res. Express, 2018, 6 (1), 016302 (1-5).

[7] S. ullah Rather, O. M. Lemine. Effect of Al doping in zinc ferrite nanoparticles and their structural and magnetic properties. J Alloys Comp., 2020, 812, 152058 (1-10).

[8] S. Kakati, M. K. Rendale, S. N. Mathad. Synthesis, characterization, and applications of $CoFe_2O_4$ and M–$CoFe_2O_4$ (M = Ni, Zn, Mg, Cd, Cu, RE) ferrites: A review. Int. J. SHS, 2021, 30 (4), 189-219.

[9] R. Vishwaroop, S. N. Mathad. Synthesis, structural, W–H plot and size-strain analysis of nano cobalt doped $MgFe_2O_4$ ferrite. Sci. Sintering, 2020, 52 (3), 349-358.

[10] C. H. Vinuthna, S. Raju, D. Ravinder. Composition dependence of elastic moduli of mixed cobalt–zinc ferrites prepared by citrate precursor method. Asian J. Chem., 2020, 32 (1), 31-35.

[11] R. C. Bharamagoudar, A. S. Patil, Sh. Mathad. Structural, dielectric, and magnetic properties of SHS-produced copper–zinc nanoferrites. Int. J. SHS, 2021, 30 (4), 241-245.

[12] M. Rostami, M. Moradi, R. S. Alam, R. Mardani. Characterization of magnetic and microwave absorption properties of multi-walled carbon nanotubes/Mn–Cu–Zr substituted strontium hexaferrite nanocomposites. Mater. Res. Bull., 2016, 83, 379-386.

[13] M. N. Akhtar, A. B. Sulong, M. N. Akhtar, M. A. Khan. Systematic study of Ce^{3+} on the structural and magnetic properties of Cu nanosized ferrites for potential applications. J. Rare Earths, 2018, 36 (2), 156-164.

[14] P. Thakur, P. Sharma, J.-L. Mattei, P. Queffelec, A. V. Trukhanov, S. V. Trukhanov, L. V. Panina, A. Thakur. Influence of cobalt substitution on structural, optical, electrical and magnetic properties of nanosized lithium ferrite. J. Mater. Sci.: Mater. Electr., 2018, 29 (19), 16507-16515.

[15] A. Jeidd, M. Amghar, A. M. Benali, A. Trabelsi, E. Dhahri, K. Khirouni, B. F. O. Costa. Study of physical properties of the $Li_{0.5}MgFe_{1.5}O_{3.5}$ ferrite nanoparticles. RSC Adv., 2023, 13 (19), 12906-12916.

[16] R. Vishwarup, A. B. Kulkarni, S. R. Manohara, S. N. Mathad. Influence of zinc doped structural properties of nano-$MgFe_2O_4$ ferrites synthesized by Co-precipitation method. Macromol. Symp., 2021, 400, 2100088 (1-6).

[17] M. A. Dar, K. M. Batoo, V. Verma, W. A. Siddiqui, R. K. Kotnala. Synthesis and characterization of nano-sized pure and Al-doped lithium ferrite having high value of dielectric constant. J. Alloys Comp., 493 (1-2), 553-560.

[18] R. N. Jadhav, S. N. Mathad, V. Puri. Studies on the properties of $Ni_{0.6}Cu_{0.4}Mn_2O_4$ NTC ceramic due to Fe doping. Ceram. Int., 2012, 38 (6), 5181-5188.

[19] R. C. Kambale, P. A. Shaikh, C. H. Bhosale, K. Y. Rajpure, Y. D. Kolekar. The effect of Mn substitution on the magnetic and dielectric properties of cobalt ferrite synthesized by an autocombustion route. Smart Mater. Struct., 2009, 18 (11), 115028 (1-5).

[20] R. C. Bharamagoudar, J. V. Angadi, A. S. Patil, L. B. Kankanawadi, S. N. Mathad. Structural and dielectrical studies of nano Mn–Zn ferrites prepared by combustion method. Int. J. SHS, 2019, 28 (2), 132-136.

[21] S. S. Khemalapure, P. L. Hosamani, S. N. Mathad, A. S. Pujar, C. S. Hiremath, P. R. Jeeragal, S. S. Pawar, R. B. Pujar. Synthesis, structural and dielectric properties of Ni–Zn–Cu ferrites. Int. J. Adv. Sci. Eng., 2019, 6 (2), 1285-1290.

[22] A. M. Bhavikatti, S. Kulkarni, A. Lagashetty. Evaluation of AC conductivity and dielectric behavior of cobalt ferrite. Int. J. Eng. Sci. Technol., 2014, 3 (7), 5985-5991.

[23] C. G. Koops. On the dispersion of resistivity and dielectric constant of some semiconductors at audio-frequencies. Phys. Rev., 1951, 83 (1), 121-124.

[24] S. N. Mathad, R. N. Jadhav, R. P. Pawar, V. Puri. Dielectric spectroscopy and microwave conductivity of bismuth strontium manganites at high frequencies. Electr. Mater. Lett., 2013, 9 (1), 87-93.

[25] M. Kaur, P. Kaur, S. Bahel. Study of magnetic, elastic and Ka-band absorption properties of $Zn_{1-x}Co_xFe_2O_4$ ($0.00 \leq x \leq 1.00$) spinel ferrites. Mater. Sci. Eng. B, 2023, 297, 116736 (1-5).

[26] A. Hriishu, M. Maisnam. Frequency dependence studies of dielectric, impedance and permeability properties of Y^{3+} substituted $Li_{0.5}Zn_{0.1}Ti_{0.1}Fe_{2.3}O_4$ ferrites. Mater. Today Proc., 2023, 92-2, 1471-1476.

[27] H. Shashidharagowda, Sh. N. Mathad. Synthesis, structural, vibrational, magnetic characterization of copper substituted cobalt manganite nano particles. Sci. Sintering, 2021, 53 (4), 429-444.

[28] R. Patil, M. K. Rendale, S. N. Mathad, R. B. Pujar. Electrical and magnetic properties of Cd^{+2} doped Ni–Zn ferrites. Inorg. Nano-Met. Chem., 2017, 47 (8), 1145-1149.

 https://doi.org/10.52340/ns.2022.23.24.03